

# The Energetic Particle Telescope (EPT) on Board PROBA-V: Description of a New Science-Class Instrument for Particle Detection in Space

Mathias Cyamukungu, *Member, IEEE*, Sylvie Benck, Stanislav Borisov, Ghislain Grégoire, Juan Cabrera, Jean-Luc Bonnet, Bart Desoete, Frank Preud'homme, Christophe Semaille, Glenn Creve, Juergen De Saedeleer, Stijn Ilsen, Luc De Busser, Viviane Pierrard, Sabrina Bonnewijn, Jeroen Maes, Emiel Van Ransbeeck, Eddy Neefs, Joseph Lemaire, Eino Valtonen, Risto Punkkinen, Michel Anciaux, Karim Litefti, Nicolas Brun, Dirk Pauwels, Cyril Quevrin, Didier Moreau, Anuschka Helderweirt, Wojtek Hajdas, and Petteri Nieminen

**Abstract**—This paper provides a detailed description of the Energetic Particle Telescope (EPT) accommodated on board

Manuscript received July 14, 2014; revised September 12, 2014; accepted September 30, 2014. Date of publication December 04, 2014; date of current version December 11, 2014. The EPT concept was originated at the Université catholique de Louvain / Center for Space Radiations CSR/UCL (Belgium), and the instrument was manufactured by a consortium comprised of QinetiQ Space (Belgium; Prime), Belgian Institute for Space Aeronomy (BISA, Belgium), and ABOA Space Research Oy (ASRO, Finland), together with UCL/CSR (Belgium), under ESA GSTP contracts for EPT Phase A/B, 20294/06/NL/JD, and Phase C/D, 22582/09/NL/AT and supported by the Belgian Federal Science Policy Office (BELSPO).

M. Cyamukungu, S. Benck and S. Borisov are with Université catholique de Louvain, Center for Space Radiations, Chemin du Cyclotron 2, B-1348 Louvain-la-Neuve, Belgium (e-mail: mathias.cyamukungu@uclouvain.be).

Gh. Grégoire, retired, was with the Institut de recherche en mathématique et physique, Université catholique de Louvain, Chemin du Cyclotron 2, B-1348 Louvain-la-Neuve, Belgium, and the Center for Space Radiations, Belgium.

J. Cabrera is with Institut de recherche en mathématique et physique, Université catholique de Louvain, Chemin du Cyclotron 2, B-1348 Louvain-la-Neuve, Belgium and at time of EPT development was with the Center for Space Radiations, Belgium (e-mail: juan.cabrera@uclouvain.be).

J.-L. Bonnet is retired from Institut de recherche en mathématique et physique, Université catholique de Louvain, Chemin du Cyclotron 2, B-1348 Louvain-la-Neuve, Belgium.

B. Desoete, S. Ilsen, G. Creve, L. De Busser and F. Preud'homme are with QinetiQ Space, Hogenakkerhoekstraat 9, B-9150 Kruikebeke, Belgium (e-mail: bart.desoete@qinetiq.be).

J. De Saedeleer is with DS Consultancy bvba, Dalstraat 8, B-1761 Roosdaal, Belgium, and also with QinetiQ Space, Belgium.

Ch. Semaille is with Thales Alenia Space, Leuven, Belgium. He was with QinetiQ Space, Belgium.

V. Pierrard J. Maes, E. Van Ransbeeck (retired), E. Neefs and S. Bonnewijn are with the Belgian Institute for Space Aeronomy (BISA), B-1180 Brussels, Belgium (e-mail: viviane@aeronomie.be).

J. Lemaire, retired, was with the Université catholique de Louvain, Center for Space Radiations, Chemin du Cyclotron 2, B-1348 Louvain-la-Neuve, Belgium, and the Belgian Institute for Space Aeronomy (BISA), B-1180 Brussels, Belgium.

E. Valtonen is with the Department of Physics and Astronomy, University of Turku, FI-20014 Turku, Finland, and also with Aboa Space Research Oy, Tierankatu 4, FI-20520 Turku, Finland (e-mail: Eino.Valtonen@asro-space.com).

R. Punkkinen is with the Department of Information Technology, University of Turku, FI-20014 Turku, Finland (e-mail: risto.punkkinen@utu.fi).

M. Anciaux, K. Litefti, N. Brun, D. Pauwels, C. Quevrin, D. Moreau and A. Helderweirt are with Belgian User Support and Operations Centre (B.USOC), BISA, B-1180 Brussels, Belgium (e-mail: Anuschka.helderweirt@aeronomie.be).

W. Hajdas is with Laboratory for Particle Physics, Paul Scherrer Institut, OBBA 010, CH-5232 Villigen, Switzerland (e-mail: wojtek.hajdas@psi.ch).

P. Nieminen is with ESA Space Environments and Effects Section, ESTEC, Keplerlaan 1, 2200 AG Noordwijk, The Netherlands (e-mail: Petteri.Nieminen@esa.int).

Digital Object Identifier 10.1109/TNS.2014.2361955

the PROBA-V satellite launched on May 7th, 2013 on a LEO, 820 km altitude, 98.7° inclination and a 10:30–11:30 Local Time at Descending Node. The EPT is an ionizing particle spectrometer that was designed based on a new concept and the most advanced signal processing technologies: it performs in-flight electron and ion discrimination and classifies each detected particle in its corresponding physical channels from which the incident spectrum can be readily reconstructed. The detector measures electron fluxes in the energy range 0.5–20 MeV, proton fluxes in the energy range 9.5–300 MeV and He-ion fluxes between 38 and 1200 MeV. The EPT is a modular configurable instrument with customizable maximum energy, field of view angle, geometrical factor and angular resolution. Therefore, the features of the currently flying instrument may slightly differ from those described in past or future configurations. After a description of the instrument along with the data acquisition and analysis procedures, the first particle fluxes measured by the EPT will be shown and discussed. The web-site located at [http://web.csr.ucl.ac.be/csr\\_web/probav/](http://web.csr.ucl.ac.be/csr_web/probav/) which daily displays measured fluxes and other related studies will also be briefly described.

**Index Terms**—Energetic particle detector, instrumentation, particle spectrometer, space radiation environment.

## I. INTRODUCTION

SPACECRAFTS, in near-Earth orbits as well as in deep space, are exposed to a complex radiation environment which is highly variable and at times very harsh. This environment consists of low energy ionospheric and plasmaspheric plasma, magnetospheric particles of intermediate energies including those forming the Ring Current during geomagnetic storms or Substorm Injection Boundary Layers, but it is also filled with energetic particles from solar events, of trapped particle belts, and of high-energy cosmic rays originating from galactic and extra-galactic sources [1]. Particle species encountered include electrons, protons, and heavy ions. This radiation is known to induce gradual material degradation and malfunction of critical electronic parts in space systems [2]–[5], but recent spacecraft failures and disturbances have been found to result also from prompt single particle events occurring with variable probability at various positions in the space radiation environment [6]–[8].

Radiation monitors are carried on board space vehicles where they operate as radiation safety devices and alert systems. The

data that they record are related to radiation doses or flux variations and can be used to take mitigation measures against radiation effects on crew and equipment whenever critical conditions are arising. Radiation monitors are compact, light and require a few watts of power budget. Sometimes, their measured quantities (counts, current, voltage, etc...) are converted into particle fluxes using rather complex procedures, the developments of which were spurred by the need to make the most of every radiation monitor given that the latter had more flight opportunities. However, limited particle discrimination capabilities, uncertainties in shielding effectiveness, poorly defined Field-Of-View (FOV) angle and the resulting inaccurate detection efficiencies, sum up to affect the level of confidence that users have, partly or entirely, in the final flux data. As a consequence, radiation monitors flux data sets are assumed to be valid when they agree with validated radiation models, but they do usually not lead to model questionings or to challenging of space radiation science, when discrepancies are revealed.

On the other hand, science-class space radiation spectrometers are developed to perform the absolute flux measurements required for scientific studies, including among others, particle acceleration mechanisms, angular distribution variations, conditions for generation of new radiation belts and particle precipitation rates. The data acquired by such kind of spectrometers are also used to validate space radiation models and in cross-calibration of radiation monitors. Science-class instruments are required to cover wide energy ranges, to achieve absolute particle type identification, to provide high energy resolution and to feature a good FOV angle definition, with less severe constraints on mass, volume and power consumption budgets. The instrument suites on the Van Allen Probes satellites perfectly illustrate what may be the targeted performances of science-class spectrometers.

The Energetic Particle Telescope (EPT) was designed to achieve performances of science-class spectrometers while requiring no more resources than earlier radiation monitors. It applies a concept [9] that allows measurements of contamination-free fluxes of particles over a relatively wide energy range, whereas the instrument fits into an envelope volume of  $127.5 \times 162 \times 211.5 \text{ mm}^3$ , has a mass of 4.6 kg and a power consumption of 5.6 Watt. Fig. 1 shows a picture of the EPT Flight Model (FM) where the stack of sensor modules can be clearly identified.

A detailed description of the EPT is provided in Section II, which also contains quantitative information on the instrument performances, its calibration, the data acquisition process and the flux extraction method. In Section III, the results of in-flight flux measurements are presented and compared to various radiation environment models. Access to the EPT data is open to the space science community under conditions that are explained in Section IV. A concluding section completes this presentation of the spectrometer and its operations on board PROBA-V (Project for OnBoard Autonomy–Vegetation).

## II. THE EPT SPECTROMETER

### A. Sensor Setup

The EPT is a charged particle spectrometer comprising 23 Passivated Implanted Planar Silicon (PIPS) detectors

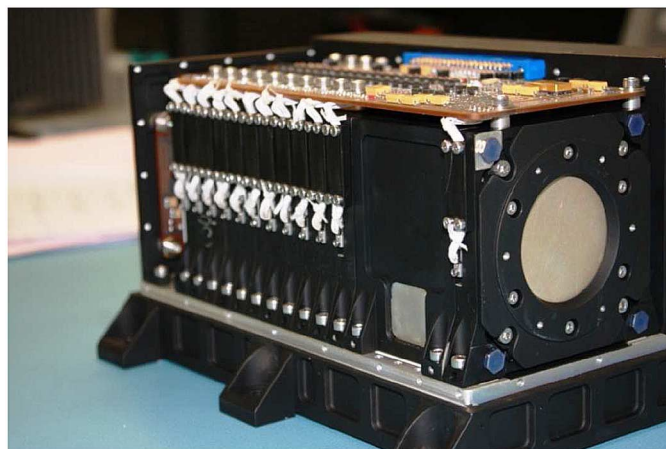


Fig. 1. Picture of the EPT FM instrument with cover removed.

( $\sim 4.5 \text{ mm}$  total thickness) mainly operating in digital mode to achieve direct particle identification and energy measurement [9]. All the detectors have a thickness of  $375 \mu\text{m}$ . A cross section view of the EPT is shown in Fig. 2, where twelve sensor modules can be clearly identified. The diameter of S1 is  $3.5 \text{ mm}$  and the outer diameter of S3 (surrounding S1) is  $35 \text{ mm}$ . S2 has a diameter of  $20 \text{ mm}$ . The front sensor modules, S1/S3 and S2 are separated by a  $50 \text{ mm}$  long serrated collimator that was designed to optimize the FOV angle definition. For most of the EPT operations, a sensor is considered as hit when it records at least  $100 \text{ keV}$  deposited energy. The S2 sensor serves as a trigger for all particle events recorded by the instrument.

The S1/S3 and S2 sensor combination constitutes the so-called Low Energy Section (LES) operated as a classical  $\Delta E - E$  telescope for the detection of low energy particles. The analogue signals from these sensors are pre-processed by a Charge Sensitive Amplifier (CSA) and a Pulse Shaping Amplifier (PSA), then digitized at  $20 \cdot 10^6$  samples per second using a 12-bit Analog-to-Digital Converter (ADC) and their pulse height is extracted and recorded by a dedicated firmware stored in a Field Programmable Gate Array (FPGA). Nine deposited energy intervals are defined for S2 (E sensor) and for each of these, four deposited energy intervals are defined in S1/S3 sensors enabling identification of electrons, protons, He-ions and any heavier ions ( $Z > 2$ ), respectively. The S1/S3 and S2 sensors also define the  $52^\circ$  FOV angle for protons ( $E < 13 \text{ MeV}$ ) since any particle has to hit both sensors in order to trigger the classification process.

The High Energy Section (HES) comprises the S2 sensor and the stack of so-called Digital and Absorber Modules (DAM). Each DAM is made of a central  $35 \text{ mm}$  diameter sensor (Fig. 2) surrounded by an anticoincidence ring (AC) of  $10 \text{ mm}$  width; an energy degrader material (tungsten or aluminum) is accommodated in front of the central sensor. In order to perform the identification of incident particles along with energy channel determination, the energy deposited in S1/S3 and S2 as well as the bit pattern generated by hit DAMs are used. In principle, the energy deposited in S2 would be sufficient for particle identification, but in order to provide full contamination-free spectra, a particle is recorded by the EPT HES only if its identification

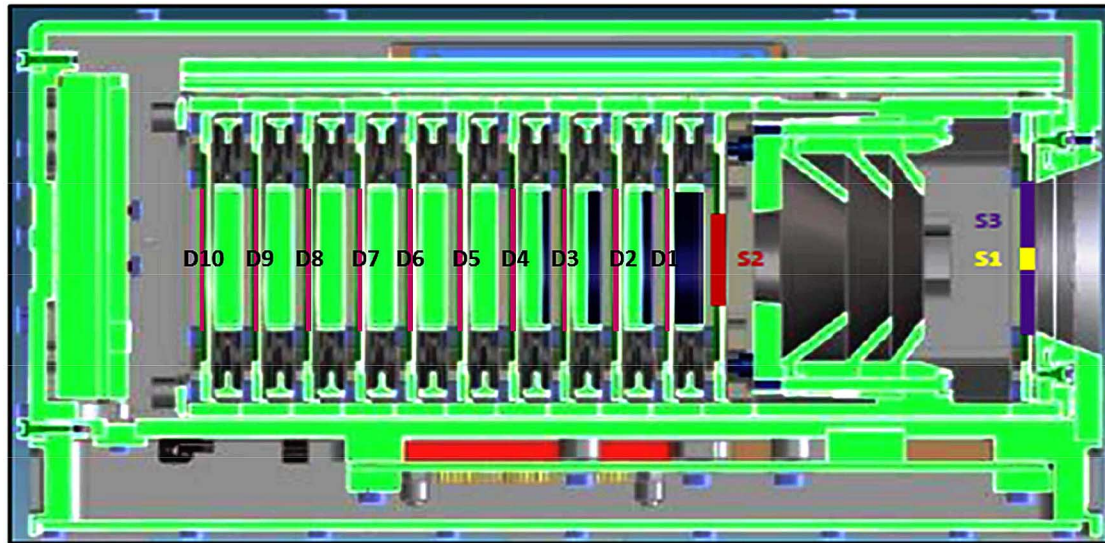


Fig. 2. Cross section view of the EPT instrument showing the collimator and the sensor layout. The S1, S2 and S3 detectors that define the  $52^\circ$  F.O.V angle are highlighted, as well as the 10 DAM detectors defining the High Energy Section (HES).

by S2 is confirmed by S1/S3. Each of the 10 possible uninterrupted series of hit DAMs defines a HES channel (when registering the last DAM hit, all the preceding DAMs need also to be hit). For particles detected by the HES, the FOV angle decreases with increasing number of hit DAMs, down to  $24^\circ$  for protons ( $E > 248$  MeV) hitting up to the last DAM.

The front window of the EPT is composed of a  $200 \mu\text{m}$  aluminum foil, which in addition to the S1/S3 thickness, sets the lower limits of incident energies to 0.5 MeV, 9.5 MeV and 38 MeV, for electrons, protons and He-ions, respectively. The upper limits of incident particle energies are then defined by the number of DAMs and their corresponding absorber characteristics (thickness and material).

For practical applications, the EPT user needs to define the instrument as a spectrometer equipped with 76 energy channels (19 channels for four types of particles) for particles detected through S1 and the same number of channels for particles detected through S3. These 152 channels are defined through deposited energy limit settings (for S1, S2 and S3) or by DAM absorber material selection and thus called “Physical Channels” (PC). Operational parameters (integration time, energy channel limits, etc...) are uploaded to the S/C and then loaded into the instrument registers at measurement start time. The EPT functional performances are described with more details in the next section.

### B. Performances

**Maximum Flux:** One of the most important requirements for the EPT is its capability to measure particle fluxes as high as  $10^7 \text{ particles}/(\text{cm}^2\text{s})$ . Based on efficiency calculations performed using GEANT4 [10], it was estimated that such a flux corresponds to a  $10^5 \text{ particles}/\text{s}$  hit rate on the front sensors S1/S3 if flux isotropy is assumed. Thereby, the PSAs were designed to provide  $\leq 10 \mu\text{s}$  pulse width, which ensures that the pile-up rate is kept  $\leq 10\%$  for the above mentioned hit rate [11].

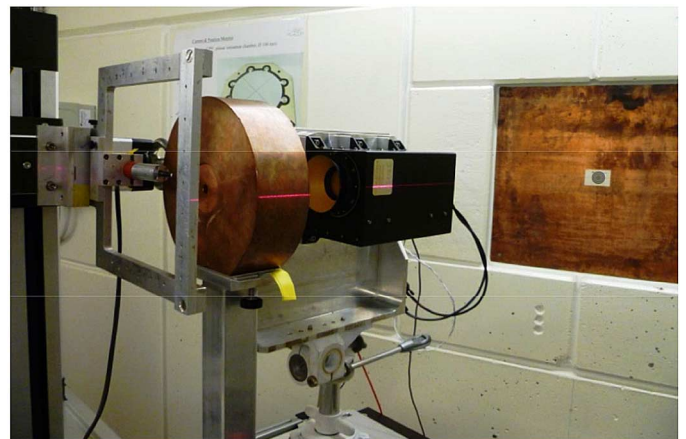


Fig. 3. Image of the experimental set-up showing the diode-based intensity monitor, the 7 cm thick collimator and the EPT.

The validation of the EPT capabilities for high flux measurements was carried-out using a 103 MeV proton beam at the Proton Irradiation Facility (PIF) - PSI Zürich. The 103 MeV protons were used because they deposit  $\sim 400 \text{ keV}$  in the  $375 \mu\text{m}$  thick S1/S3 sensors, generating pulses that are typically similar to that of electrons, which often dominate high count measurements in space environment.

The experimental setup used during the EPT FM calibration and validation is shown in Fig. 3. It is comprised of a set of Copper-based energy degraders followed by a diode-based intensity monitor, a 7 cm thick, 1 cm inner diameter Cu collimator and the EPT. Before each data acquisition with a selected energy (defined by the thickness of the degrader), the diode-based intensity monitor is calibrated by a scintillator-based detector that is placed at the location of the EPT. For the data acquisition at 103 MeV protons, no degraders were used.

The variation of the intensity of detected 103 MeV protons as a function of the incident beam intensity (measured by the calibrated diode-based intensity monitor) is shown in Fig. 4. The

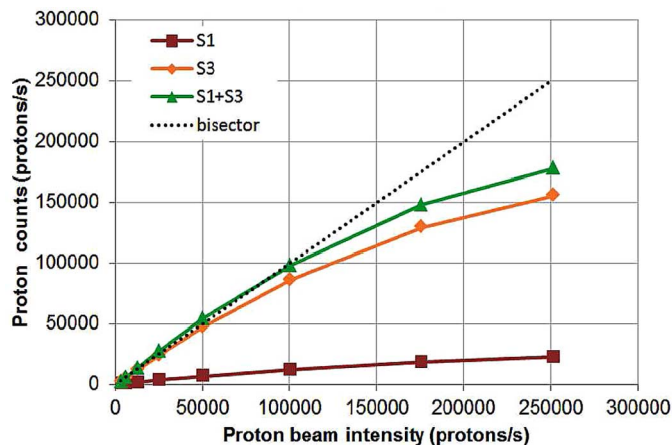


Fig. 4. EPT measured counts (50th-percentile) as a function of 103 MeV proton beam intensity.

measured counting rate follows a straight line up to an incident intensity of about  $10^5$  protons per second.

As the S3 detector has a surface 100 times larger than the S1 sensor, the impact rate that it registers in an isotropic field is about 2 orders of magnitude higher than the rate in S1 and therefore it is more sensitive to pile-up than S1. Consequently under extreme conditions when the particle flux incident on the instrument aperture exceeds the  $10^5$  particles/s limit, a correction factor which is a function of S1 count rate should be applied to derive the final total S1 + S3 count rate for use in the flux extraction procedure. Even though excessively high fluxes have not been encountered during the one year EPT operations, the current margin on noise could be used to decrease the pulse width at the PSA level, so as to increase the EPT upper flux limit if deemed necessary in other missions. Indeed, the EPT modularity also allows that fast scintillator-based S1/S3 modules (ensuring  $\leq 100$  ns PSA pulse width) can be used if a rugged thin scintillator technology could be qualified for space applications.

**The Energy Calibration:** The energy calibration of the sensors was performed with a proton beam of energy 202.5 MeV and intensity of approximately  $2.5 \times 10^4$  p/cm<sup>2</sup>/s (Beam current: 0.2 nA, initial proton beam energy: 230 MeV, degrader: 10 mm of Cu, temperature: 25°C).

The energy deposited by 203 MeV protons in the EPT FM sensors was obtained by GEANT4 simulation and is shown in Fig. 5 for the three front sensors. For the S1, S2 and S3 sensors these values are  $260 \pm 20$  keV,  $270 \pm 20$  keV and  $260 \pm 20$  keV, respectively. It is assumed that at 203 MeV, the energy deposited is practically the same in all the analog sensors, and that the observed 270 keV in S2 is due to statistical fluctuations rather than to its position downstream in the beam. Thereby, an average value of 263 keV is considered as deposited energy in the analog sensors. For S2, this value was compared to the experimental pulse height histograms (blue) shown in Fig. 6. The Most Probable Value (MPV) of pulse height in S2 is estimated to be  $25 \pm 3$  ADC units by the Landau distribution fit (red), though the experimental peak occurs at higher value. Based on these results, it can be concluded that the lower limit of the calibration constant is  $25/263 = 0.095 \pm 10\%$  ADC LSB/keV.

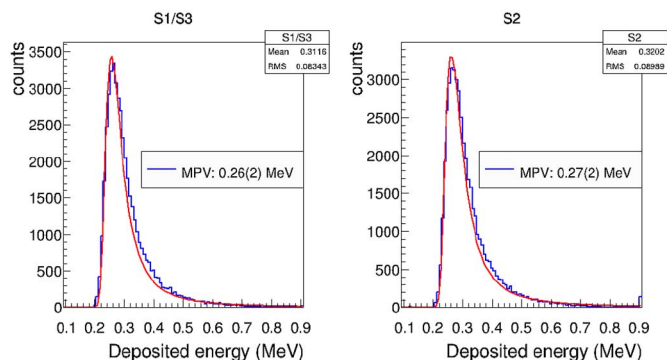


Fig. 5. Histograms of counts as a function of energy deposited in S1/S3 and S2 sensors (blue) with fits by a Landau distribution (red): The Most Probable Value (MPV) is shown in the insets along with their uncertainties.

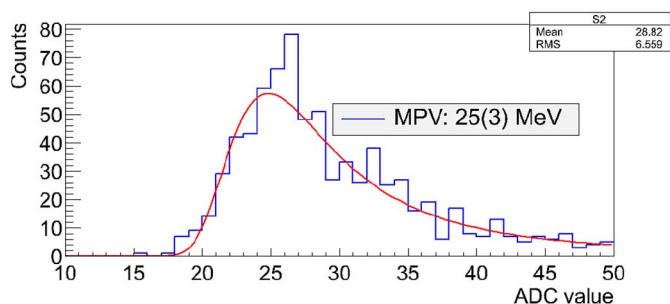


Fig. 6. Experimental deposited energy histogram (blue) for S2, in terms of counts as a function of pulse height ADC value. The Landau distribution fit (red) of the experimental histogram defines the MPV.

The same 203 MeV beam was used to find the calibration constant for the DAM and AC detectors. It was measured using a differential method (instead of pulse height extraction) that allows better statistics. This method is imposed by the instrument, as the DAM signals are not converted into digital values by an ADC but only give a digital pulse once their height exceeds a preset threshold given by a DAC (Digital to Analogue Converter). Fig. 7 shows as an example the results obtained for DAM3. As a result of this measurement campaign the calibration constant for the DAM detectors was found to be 23 DAC LSB/100 keV.

The possible variation of calibration constants as a function of temperature was investigated using the S2 sensor. In fact, the EPT is equipped with three sensors that record the temperatures a few millimetres above the S2 sensor (at the bottom layer of the PSA PCB), on the Power Conditioning Unit (PCU) board in the bottom compartment of the instrument and on the Data Processing Unit (DPU) board beside the DAM stack. The EPT was introduced in a thermostatic bath and the calibration constants were measured at three temperature values in the  $-10^\circ\text{C}$  to  $30^\circ\text{C}$  range. It was found that the temperature effect on the energy measured by the S2 analogue channel is  $< 10$  keV/ $40^\circ\text{C}$ , which is actually considered as negligible, since the in-flight EPT temperature is within the  $0^\circ\text{C}$  to  $25^\circ\text{C}$  range.

In-flight calibration of the EPT is possible for the three analogue channels through the determination of the maximum energy deposited by protons in the LES sensors. It was not

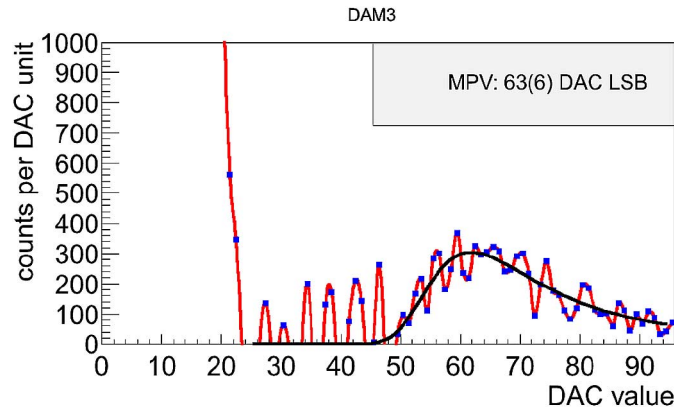


Fig. 7. Experimental spectrum (red line, blue dots) representing differential counts as a function of energy deposited by 203 MeV protons in the DAM3 (expressed in DAC value) with Landau distribution fit (black).

TABLE I  
ENERGY LIMITS (IN MeV) OF THE VIRTUAL CHANNELS (VC) FOR EACH PARTICLE TYPE

VC	Electrons	Protons	He-ions
1	0.5-0.6	9.5-13	38-51
2	0.6-0.7	13-29	51-116
3	0.7-0.8	29-61	116-245
4	0.8-1.0	61-92	245-365
5	1.0-2.4	92-126	365-500
6	2.4-8.0	126-155	500-615
7	8.0-20	155-182	615-720
8		182-205	720-815
9		205-227	815-900
10		227-248	900-980
11		>248	>980

found necessary to provide the DAM channels with re-calibration functions since these sensors are heavily shielded and it was noticed that slight drift of their gain does not significantly affect the EPT efficiencies.

*The Detection Efficiency of EPT Channels:* Each EPT physical channel contains only one type of particle. For that particle, the efficiency matrix provides quantitative information on the contribution of a given incident energy interval to the counts observed in a physical channel. Such energy intervals are called “Virtual Channels” (VC) and serve as a basis to define the abscissa of energy spectra. They are shown in Table I for each of the particle species that the EPT can identify.

The GEANT4 tool was used to evaluate the intrinsic detection efficiency matrix (i.e. the probability for a particle from a given virtual channel to be detected in a given physical channel provided that it has crossed the detector aperture towards EPT). About one billion events of each particle type (electrons in the energy range 0.1–20 MeV, protons in the energy range 5–300 MeV and He-ions in the energy range 20–1600 MeV) were tracked from the 78 mm diameter EPT aperture defined as the base of the Al cone used to fit the instrument into the through hole in the satellite panel. The flux of energetic particles at LEO is highly anisotropic [12]–[14]. However, in

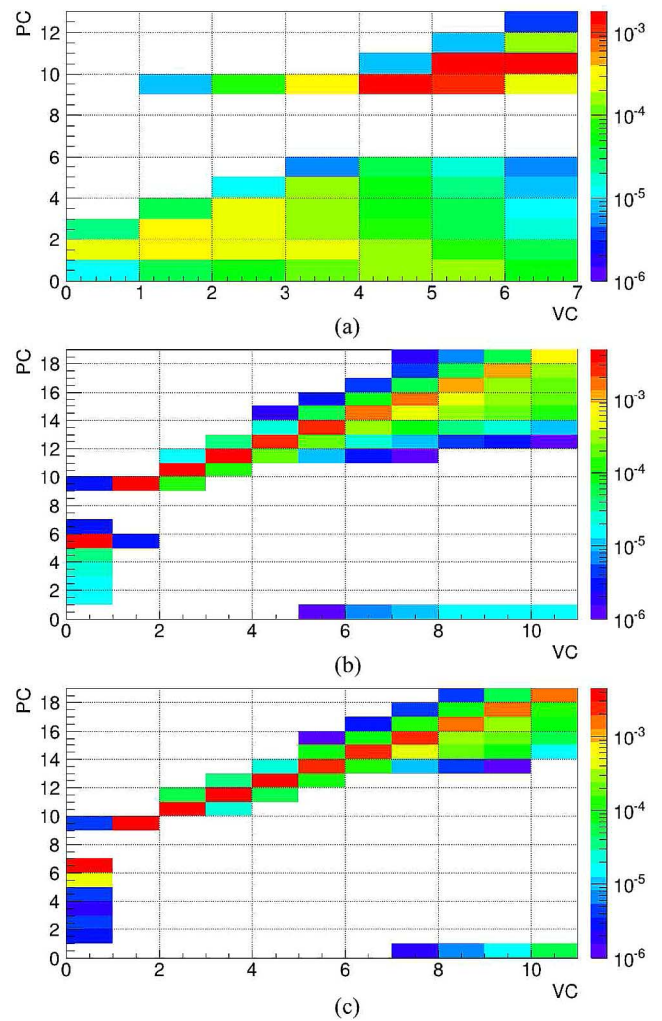


Fig. 8. Graphical representation of the particle efficiency matrices: (a) electrons, (b) protons, (c) He-ions.

order to extract zero order flux approximations [15] to be compared with existing data set or models, the detection efficiency calculations were performed for particle fluxes assumed to be isotropic over the half-hemisphere in front of the EPT and the impact positions were uniformly distributed over the aperture [16][9]. Analyses of angle-dependent fluxes are underway [17] and their description is outside the scope of this paper.

Graphical representations of the particle efficiency matrices are shown in Fig. 8. For electrons only 13 physical channels (PC) are shown as it was observed that there are no events registered in the upper channels. The first 9 channels for each particle which correspond to the LES, were defined so that the first and last channel should always be empty for each particle type.

The energy limits of the virtual channels (VC) were defined so as to match the best with the physical channels imposed by the instrument characteristics. The matrices for protons and He-ions are highly diagonal which allows a quick interpretation of the counts observed in their physical channels and a quasi-straightforward conversion to fluxes.

The intrinsic detection efficiency of protons was qualitatively assessed through the measurements of beam particle spectra obtained at various incident energies between 22 and 202 MeV.

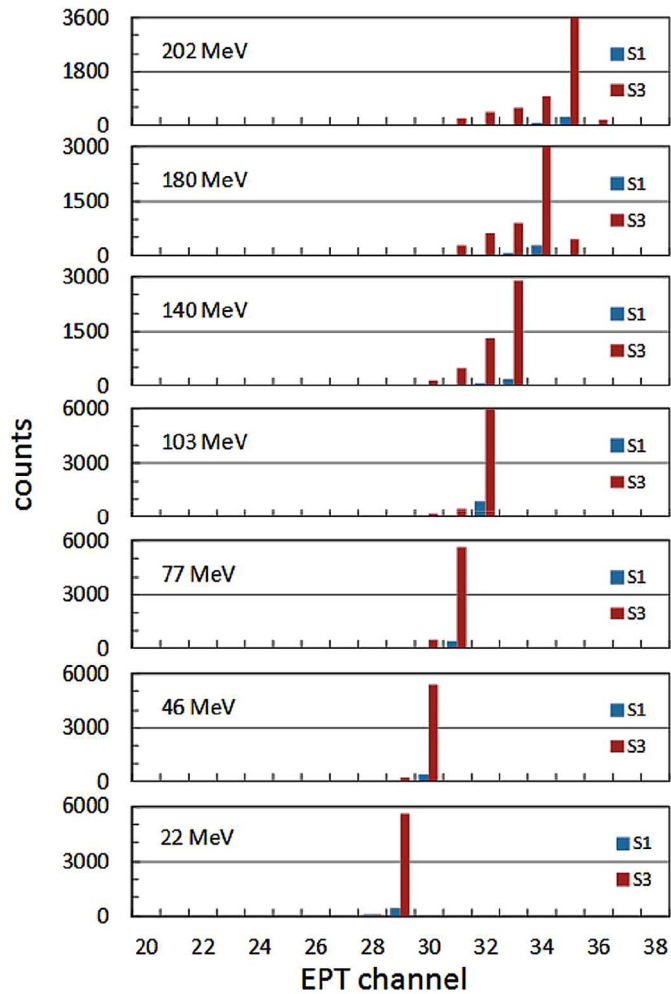


Fig. 9. Detection of protons with various incident energies in the different EPT channels.

Even though the accelerator beam could not mimic an isotropic flux, the performed measurements demonstrated that protons were counted in their predicted channels.

Fig. 9 shows the detection of protons with different incident energies in the corresponding EPT channels. As an illustration, it can be observed that almost all the 46 MeV protons (proton VC = 3, Table I) are detected in the 11th PC (EPT channel 30) as predicted by the efficiency calculation results shown in Fig. 8(b). Not only the same channel correspondence has been validated for the other incident energies, but also the capability of the EPT to never count protons in the electron and heavy ion channels was confirmed [9].

An equivalent validation campaign was conducted with He-ions at KVI-Groningen and the results were quite similar: particles are detected in their dedicated channel and no inter-particle contamination was observed.

*The EPT Field of View Angle:* In order to validate its angular opening, the EPT (EQM) was rotated around an horizontal axis drawn onto the aperture plane. The angle between the proton beam and the EPT principal symmetry axis was varied from 0 to 30° by steps of 2° or 5° for 105 MeV or 21.8 MeV incident protons, respectively. For 105 MeV protons, the contents of channel 32, 31 and 30 (see Fig. 9) were recorded at various

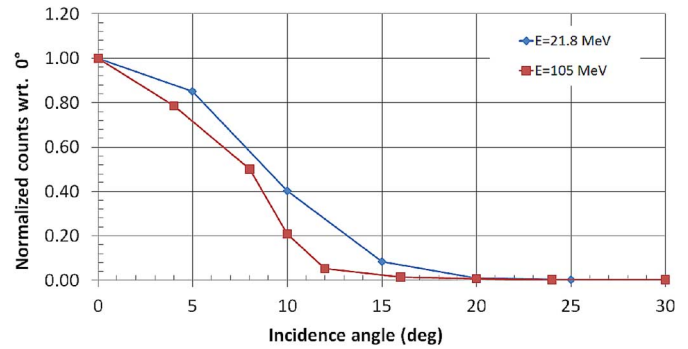


Fig. 10. Angular variation of EPT counts for 21.8 and 105 MeV protons.

angles, whereas the content of channel 29 was recorded as a function of incidence angles for protons with incident energy of 21.8 MeV. Fig. 10 shows the variations of the measured EPT counts for both incident energies as a function of the incidence angle. For these energies, the determination of the FOV angle by GEANT4 simulations predicts that 99% of the particles detected come from trajectories where the incidence angle is below 16 or 21 degrees for 105 MeV or 22 MeV protons, respectively, which is in good agreement with the measurements.

This measurement confirms that protons that are by more than 26 degrees off-axis (LES) are not detected by the EPT and that the high energy protons (HES) which deeply penetrate into the EPT are detected from a much lower FOV. For protons and ions, the EPT can be considered as a directional spectrometer, in spite of its capabilities to measure omnidirectional fluxes in specific conditions (for example when the angular distribution is not too narrow and EPT is looking towards the direction of maximum flux intensity). However, for the electrons it was calculated [9] and qualitatively observed (with a strontium electron source) that they may be detected even with 55° incidence angle since they are scattered by the entrance window sheet. For electrons, the detection FOV also decreases with increasing energy.

Finally, by rotating and shifting the EPT, it was shown that 203 MeV protons impinging the instrument through the sides are not counted in the particle channels.

*The Configuration File:* The EPT operations are driven by parameters that are stored in a configuration file and uploaded to PROBA-V at its pass over the Mission Control Center in Redu, Belgium. The configuration file is transferred to the EPT at the beginning of every measurement, which has a typical duration between 1 and 10 hours. The configuration file contains over 400 parameters defining the deposited energy limits for particle selection and energy channel identification, the sensor bias high voltages, a sensor validity mask that indicates defective DAMs, the deposited energy thresholds for the sensors, the integration time (normally set to 2 seconds) for data acquisition, as well as some signal processing-related parameters. This makes of the EPT a reconfigurable instrument that can be kept operational even in case of sensor degradation or complete failure, or in case of excessive noise increase. During the commissioning phase that lasted from 16 May to 3 July 2013 the configuration file was optimized so as to guarantee the best particle discrimination capability and channel definition, and since 24 June 2013 the data are acquired with this optimized configuration.

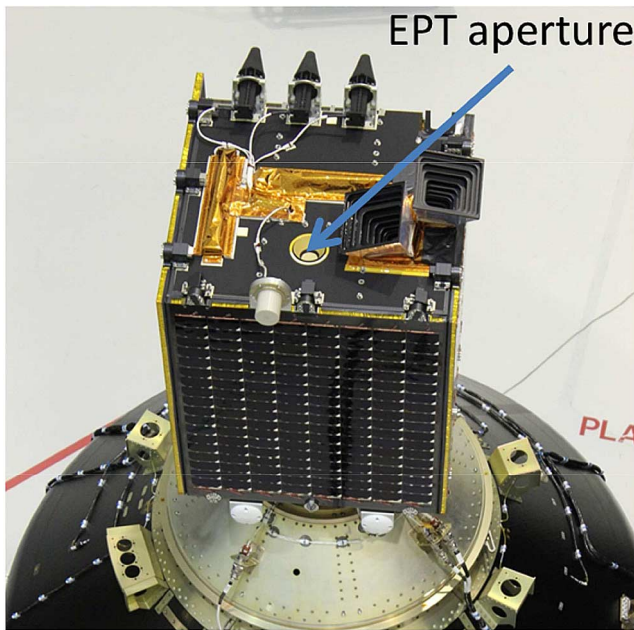


Fig. 11. View of the PROBA-V satellite mounted on the launcher with tagged EPT aperture.

**Health Check of the Instrument:** While the detection of coincident signals in the sensors allows accurate particle classification, the signal counting rate from each individual sensor is used to check the quality of the measurement. In fact, these counting rates allow to determine when saturation of the sensors needs to be taken into account for data analysis or when registered measurement has to be rejected due to abnormal noise. In fact, while proton flux measurements are immune to most of the instrument disturbances, electron flux measurements in presence of intense flux of high LET particles (dominated by low energy protons mainly in the SAA and during SEP event) was found to be disturbed sometimes: The origin is an increase in electric current induced by the high LET particles and generating transient baseline variations. Such baseline variations make that some signals in the analogue sensors are interpreted as valid events during a few tens of microseconds. Although the duration of the transient noise is negligible as compared to the 2 seconds nominal integration time of the EPT, these events result in anomalous count rates. Finally, any measurement in which disturbances occur on sensor counting rates and on baseline levels is discarded at data analysis time.

### C. The EPT On-Board PROBA-V

The PROBA-V satellite with the EPT as technology demonstration instrument on board was launched on the 7th May 2013 by a Vega Rocket from Kourou–French Guyana (Fig. 11). The satellite primary mission is Earth vegetation imaging, it is three-axis stabilized and it circles on a Sun-synchronous LEO polar orbit with the following characteristics: altitude: 820 km, inclination: 98° and local time at the descending node: 10:30–11:30 AM, period: 101 min.

The EPT on board the PROBA-V satellite is oriented WEST when in daylight and oriented EAST when in eclipse. The angle between its boresight direction and the local magnetic

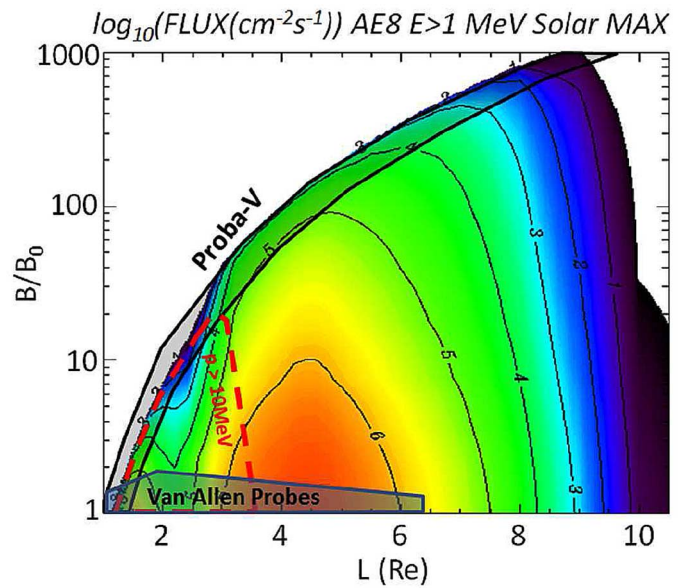


Fig. 12. Invariant coordinate map ( $L$ ,  $B/B_0$ ) of the AE-8 MAX integral electron flux  $> 1$  MeV. The position of the belt of  $> 10$  MeV protons is indicated in red. The region covered by the PROBA-V satellite is indicated in black. For comparison the region covered by the Van Allen Probes (blue) is also shown.

field varies between 60° and 120°, i.e. around 90°, when no off-pointing of PROBA-V is performed for specific operational reasons or some scientific investigations as for example pitch angle distribution studies. The angle between the instrument boresight direction and the local magnetic field is assumed to give the average particle pitch-angle over the FOV in the inertial reference system and it can be obtained through two methods: i) The PROBA-V onboard magnetometer measures the three components of the local magnetic field in the spacecraft fixed body of frame (BOF). In orbit, the satellite X-axis is oriented in the direction of its velocity vector, its Z-axis is oriented towards the Earth and the Y-axis is oriented perpendicular to X and Z in the direction according to the right-hand rule. The boresight direction of the EPT is parallel to the Y-axis and therefore its average pitch-angle can be readily evaluated. ii) The EPT data exploitation team has access to the commanded attitude data in terms of quaternions and using the calculated magnetic field (based on extrapolated IGRF2010 and external magnetic field Olson–Pfitzer quiet) the average pitch angle can be determined. Both methods are generally in good agreement with each other except during commanded attitude changes.

As consequence of its Low Earth Orbit, the EPT samples the Radiation Belts near their low altitude edges. Fig. 12 shows the location of the radiation belts as defined by  $> 1$  MeV electrons on an invariant coordinate map [18]. The region covered by the PROBA-V satellite is indicated inside the thick black contour (Note that a more adequate invariant coordinate system should be used to map the steep flux gradients in the LEO region with better resolution [19]). For comparison, the region covered by the Van Allen Probes (launched in August 2012) is also shown. The particle flux measurements performed on board PROBA-V and the Van Allen Probes can be considered as complementary, but also are used for cross-validation of fluxes measured in the overlapping regions.

#### D. The Data Acquisition

The EPT data are continuously acquired and stored in the PROBA-V host memory from where they are downloaded to the ESA satellite Mission Control Center (MCC) in Redu, Belgium at S-band passes every 1 h 30-3 h 30 or 8 h-14 h. The EPT data are then complemented with the ephemeris data and transmitted to the Belgian User Support and Operation Center (B.USOC) for decommutation and primary validation. The so-called L0 data which undergo a primary validation are time series comprised of measured counts along with satellite coordinates and EPT housekeeping information. Upon successful validation, the L0 data are transmitted to the EPT Data Center at UCL - Center for Space Radiations (UCL/CSR) for a final validation and flux extraction. The extracted fluxes are stored as L1 data files at UCL and B.USOC from where they can be accessed for use in science and engineering-related studies that are performed in parallel with further data quality control. The data extraction procedure is described in more details in the following section. A high degree of autonomy is built into the EPT operations, allowing maximum flexibility for the user, while providing maximum operational availability. Although, the EPT data acquisition is temporarily interrupted before data transmission (which results in a reduced number of data around the Redu station), the EPT is active for > 96.5% of the time.

#### E. The Flux Extraction

Inside the  $2 \times 76$  EPT channels that register counts, the identification of particle types is already performed and the information from a set of 19 physical channels (PC) can be attributed to each type for incident spectra extraction (VC).

Converting the measured counts in PCs into integral fluxes over the VCs amounts to searching for an approximate solution of the system of linear equations:

$$\begin{pmatrix} a_{00} & \dots & a_{(N-1)0} \\ \dots & \dots & \dots \\ a_{0(K-1)} & \dots & a_{(N-1)(K-1)} \end{pmatrix} \cdot \begin{pmatrix} V_0 \\ \dots \\ V_{N-1} \end{pmatrix} = \begin{pmatrix} P_0 \\ \dots \\ P_{K-1} \end{pmatrix} \quad (1)$$

where  $a_{ij}$  is the efficiency to detect a particle of the  $i$ -th VC (labelled  $V_i$ ) in  $j$ -th PC (labelled  $P_j$ ). For the labelling of an element  $a_{ij}$  in the efficiency matrix,  $i$  refers to the column number and  $j$  to the line number. The total number of PCs is equal to  $K$  and the total number of VCs is equal to  $N$ . It is clear that a unique solution of the system can be found when row rank of the matrix  $A = [a_{ij}]$  is greater or equal to  $N$ . But if there are 2 or more VCs that are not distinguishable at least in a single PC, a unique solution cannot be found.

If the best solution of equation (1) is known, then when it is multiplied by  $A$  and subtracted from the  $P$  vector, the residual values will be very small and in the ideal case equal to 0. So if we find some estimation of  $V$  that will decrease the residuals  $|P - P_{estimated}|$ , and we repeat it many times until the residuals of  $P$  reach minimum value at a given precision, then the set of all the estimations obtained during iterative process will be the best solution of the system.

Since there is no a-priori knowledge of  $V$ , one must use only the efficiency matrix  $A$  and the measurements  $P$  in order to provide such an estimation. For the first estimation it is assumed that the values  $V_i$  are equal (one to each other) but unknown. They can then be independently estimated from every equation (i.e. with the use of every PC measurement).  $V^j$  the estimation from the  $j$ -th equation is then given by:

$$V^j = \frac{P_j}{\sum_i a_{ij}} \quad (2)$$

Since the elements of the matrix  $A$  are all different (this is a requirement for spectra measurement), one can note that a given VC will have more important contribution to certain PCs than to the others. So, by calculating a weighted mean value for every element of  $V$  with the use of estimated  $V^j$  (2), an initial and realistic spectrum estimation can be obtained. The weight is based on the relative contribution of a given VC ( $i$ ) to a PC ( $j$ ) (first factor in (3)) and on the absolute capability of the instrument to count particles belonging to VC ( $i$ ) in the PC ( $j$ ) (proportional to efficiency  $a_{ji}$ ). Such a two-component weighting factor allows to extract the flux in a VC from the information contained in the PCs where the contribution from that VC is dominant. It is expressed as:

$$w_{ij} = \frac{a_{ij}}{\sum_i a_{ij}} \cdot a_{ij} \quad (3)$$

Then the initial spectrum estimation  ${}^0V$  is expressed as follows:

$${}^0V_i = \frac{\sum_j V^j w_{ij}}{\sum_j w_{ij}} \quad (4)$$

This expression has two key properties: (i) in case  $K = N$ , and  $A$  is a diagonal matrix ( $a_{ij} = 0$  if  $i \neq j$ ), estimation (4) gives immediately the exact solution of the system (1); (ii) the estimated values of  $V_i$  are automatically non-negative as expected for fluxes.

Equation (1) can be rewritten as follows:

$$\begin{pmatrix} a_{00} & \dots & a_{(N-1)0} \\ \dots & \dots & \dots \\ a_{0(K-1)} & \dots & a_{(N-1)(K-1)} \end{pmatrix} \cdot \begin{pmatrix} d^1 V_0 + {}^0 V_0 \\ \dots \\ d^1 V_{N-1} + {}^0 V_{N-1} \end{pmatrix} = \begin{pmatrix} P_0 \\ \dots \\ P_{K-1} \end{pmatrix} \quad (5)$$

Or, in matrix form:  $A \cdot (d^1 V + {}^0 V) = P$ , where  $d^1 V$  is the first order correction, that is now unknown. Equation (5) can be easily brought to the same form as (1):

$$A \cdot d^1 V = d^1 P \quad (6)$$

where  $d^1 P$  is expressed as follows:

$$d^1 P_j = P_j - \sum_i a_{ij}^0 V_i \quad (7)$$

Under this form, equation (6) can be treated as equation (1), and this process can be repeated many times. Actually, the algorithm will converge after a certain number of iterations if the absolute value of  $d^n P_j$  is lower than the previous one  $d^{n-1} P_j$  ( $n$  is the number of iterations).

It was tested with a large amount of trial spectra that after the first iteration, the residual counts are decreasing if statistical fluctuations are negligible.

Moreover, this algorithm was extensively tested with simulated and experimental data and no severe stability issue was found, while it was confirmed that the process always converges to a solution (residual counts steadily decreasing) when statistical fluctuations are small. However, in order to avoid any negative solutions for flux values in some VCs, which is possible in case of low statistics, one security condition was set: if the estimated flux in a VC at a given iteration is negative and its absolute value is higher than the sum of the estimations before the current iteration, this estimation is set equal to the sum of the estimations obtained before but with the negative sign, and the iterative process is continued. So in the worst case the final solution for some VCs may become zero.

When the efficiency matrix  $A$  is explicitly known, one can use its properties (e.g. if some of its elements are equal to zero or some of them are significantly higher than others) in order to impose some constraints and define immediately which members of  $V$  will be equal to zero or negligible. The efficiency matrices of EPT instrument for different kind of particles are presented in Fig. 8 and they are of two types: quasi-diagonal matrices for protons and He-ions, and highly triangular matrix for electrons.

Electrons present the most complicated situation with high overlapping tails in the efficiency matrix, i.e. with the VC number incremented by one, the corresponding higher PC becomes efficient, but the sensitivity of lower PCs is not necessarily affected. This is reflected in the electron efficiency matrix (Fig. 8) by its rather triangular shape, except for PC number 10 (which corresponds to DAM1 that is integrating a wide energy range, but in any case has the highest efficiency for VC = 5). It means that low PCs are expected to be always hit, while the highest non-zero PC can define the highest VC that will have a non-zero value.

In practice, for optimization of the system, the information in the first physical channel for each particle type is not used, as well as terms in the efficiency matrices that are below  $10^{-5}$ . For electron spectrum extraction, counts registered in electron-PC 2, 3, 4, 5, 10, 11 and 12 are used. For proton spectrum reconstruction, counts registered in proton-PC 6 and 10 to 18 are used and counts recorded in He-ions-PC 7 and 10 to 18 are exploited to obtain He-ions spectra.

Based on the above-defined parameters and variables, the spectrum reconstruction algorithm includes the following steps:

- 1) Highest non-zero PC is found; according to this the highest VC to be reconstructed is defined.

- 2) Lowest non-zero PC is found; according to this the lowest VC to be reconstructed is defined.
- 3) Weights for spectrum estimations are calculated using this restricted PC and VC range.
- 4) Spectrum estimation according to (4) is performed.
- 5) (for iterations after the first one) If some of the  $V$  components are negative and their absolute value is higher than the sum of the solutions preceding this iteration step ( $V^S$ ), its value is set to  $-V^S$ .
- 6) Residual counts in PCs according to (7) are calculated.
- 7) Correction is added to the initial estimation to get the solution vector  $V^S$ .
- 8) Operations (4–7) are repeated with the only difference that instead of measured counts, residual counts are used. The iterative process is stopped if at least one of the following conditions is satisfied:
  - a)  $\chi^2$  is less than a threshold value ( $\chi^2$  is equal to the sum of squares of residual counts divided by statistical error of initial counts), this value is set to 0.01.
  - b) At least 10 iterations are made and  $\chi^2$  is not decreasing anymore with the minimum required speed  $\eta = \chi_{n+1}^2 / \chi_n^2$  ( $n$  = iteration number). During adjustment of the algorithm the optimal value for  $\eta$  was found to be 0.9999.
  - c) The maximum allowed number of iterations (1000) is exceeded.

The statistical uncertainties on estimated fluxes are not calculated during the spectrum unfolding process, since the implied intermediate values are correlated and no straightforward information on their covariance is available. In the meanwhile, flux error estimations are based on a simplified approach that is presented hereafter.

Upon completion of the iterative flux extraction procedure, the expected contributions of a given VC to counts in any PC are calculated using the efficiency matrix. The contribution to the statistical error of the measurements from this VC in different PCs is obtained as a square root of these counts. Then, the relative error on a given VC value is calculated as weighted mean value of relative errors on counts in the PCs. Weights are equal to the respective efficiencies, i.e. the most efficient PCs contribute the most to the total VC error, while PCs with low efficiency and/or with low statistics will affect the overall statistical error in a limited way. The relative error on the extracted flux  $E(V_i)$  may be expressed as follows:

$$E(V_i) = \frac{\sum_j \frac{a_{ij}}{\sqrt{a_{ij} V_i}}}{\sum_j a_{ij}} = \frac{\sum_j \sqrt{\frac{a_{ij}}{V_i}}}{\sum_j a_{ij}} \quad (11)$$

The above-described approach leads to reasonable estimations of the statistical errors, if  $\chi^2$  values are low, i.e. if the residual counts are low. These estimations mainly represent the statistical part of the errors, while possible systematic errors originating from the procedure itself are not taken into account. As consequence, if a given flux is estimated as zero due to insufficient counts in related PCs (not zero, but not sufficient compared to the neighbour channels), its error is also estimated

to be exactly zero. This drawback of the method will be addressed later, even though in most of the cases this approach gives reasonable estimations of the accuracy of the obtained results. Therefore spectra with alternating high and zero errors should be considered as inaccurate. Moreover it should be noted that in case of high  $\chi^2$ , the resulting spectra should be considered with particular attention because the flux extraction is not perfect by itself.

This flux extraction procedure has been tested with simulated data. In order to simulate the response of the EPT to the particle fluxes along the PROBA-V orbit, the Space Environment Information System (SPENVIS) tool [20] was used to generate the expected fluxes. A sun synchronous orbit at 820 km altitude and 10:30 AM local time at descending node was calculated by the orbit generator for a period of 15 days starting on 1st April 2013. The time resolution in the generated orbit file is 1 minute. The AP8MAX and AE8MAX radiation belt models were used for proton and electron flux estimations, respectively. The flux output files from SPENVIS give integral spectra in ( $\text{cm}^{-2} \text{s}^{-1}$ ) units for various threshold energies as a function of time. These fluxes were converted into a number of hits on the EPT aperture from each VC by taking into account the geometrical factor of the entrance window ( $149 \text{ cm}^2 \text{ sr}$ ), the integral flux of each VC and the integration time of the instrument (1 second and 2 seconds, for electrons and protons, respectively). The conversion from VC counts to PC counts was readily performed by applying the efficiency matrix. Statistical fluctuations, according to a Poisson distribution, were added to the simulated PC counts and the reconstruction of the primary spectra was carried-out from these realistically fluctuated counts. Fig. 13 and Fig. 14 show comparisons between original simulated spectra (black dots) and reconstructed spectra (red triangles) deduced from PC counts with statistical fluctuations. The total number of counts available for spectrum reconstruction is indicated on top of each graph as well as the sum of the fluctuations of the counts in channels with regard to a poissonian distribution.

The quality of the reconstruction procedure increases with increasing number of total counts in all the channels. In case of electrons if a spectrum is deduced from a total of more than 500 counts in the PCs, then it can be reconstructed with an overall relative error of about 20%. For protons and He-ions, as the efficiency matrices are quasi-diagonal, the reconstruction precision is highly related to the counting statistics and the number of counts in each channel is the main parameter that determines the precision on the reconstructed flux.

### III. IN-FLIGHT FLUX MEASUREMENT RESULTS

The following section is dedicated to differential fluxes that are obtained from the EPT measurements on-board PROBA-V. The data are compared to AP8/AE8 MAX model predictions in order to draw preliminary conclusions on circumstances (positions, orientation, data acquisition configuration, etc...) under which good agreement or discrepancies between the EPT data and models are observed.

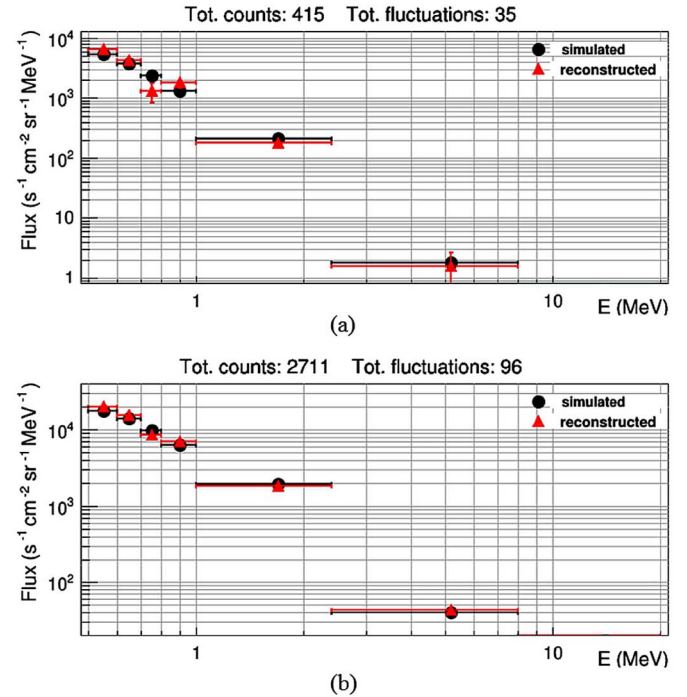


Fig. 13. Examples of comparison between original electron spectra as given by the SPENVIS tool (black dots) and reconstructed spectra (red triangles) as deduced from PC counts. The total number of counts available for spectrum reconstruction is indicated on top of each graph as well as the sum of the fluctuations of the counts in channels with regard to a poissonian distribution.

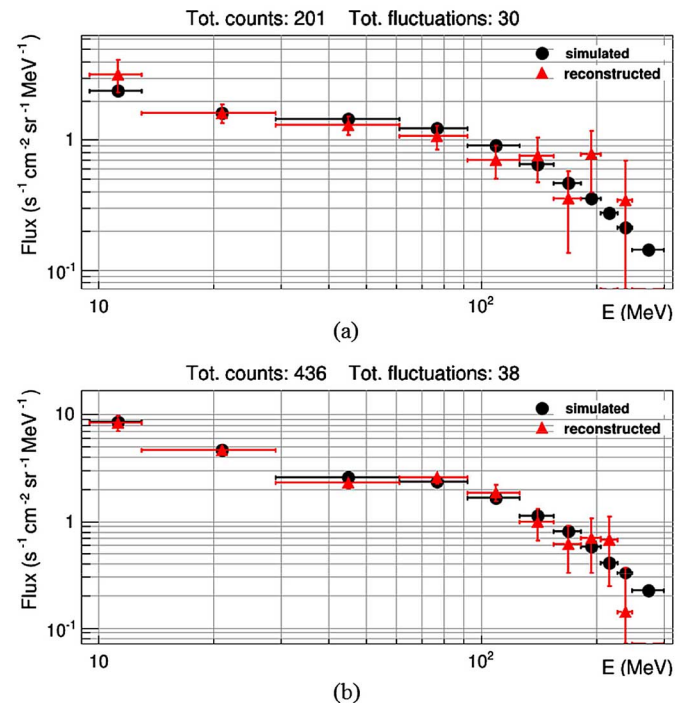


Fig. 14. Same as in Fig. 13 but in case of protons: comparison between original simulated proton spectra (black dots) and reconstructed spectra (red triangles).

#### A. Electron Spectra

Fig. 15 shows in the upper panel the count rates in the electron physical channels that have been taken into account to reconstruct the differential spectra represented in the lower panel.

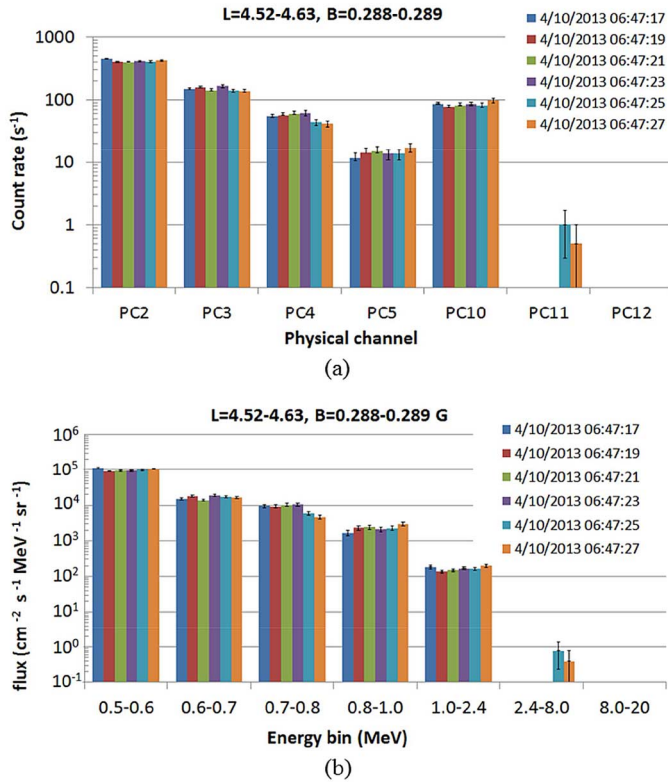


Fig. 15. (a) Physical channel spectra and (b) energy differential spectra (virtual channel spectra) as measured in the outer radiation belt (Geographic location: longitude =  $47.0 \pm 0.2^\circ$ , latitude =  $-55.6 \pm 0.3^\circ$ , altitude = 831.2 km).

Six consecutive measurements are shown at a given time in a position bin located in the outer belt. In this case, the total number of counts/second exceeds 500 and the reconstruction of the incident spectra is quite stable.

Fig. 16 shows a comparison between differential fluxes predicted by AE8MAX and the unfolded spectrum from the EPT data. The agreement is quite good taking into account that the instantaneous spectrum may vary by over an order of magnitude with geomagnetic activity conditions and that the AE8 model gives an average spectrum taken from many measurements over a large period of time [21]. In this region, during the period from 22 May to 24 November 2013, for the energy bin 0.5–0.6 MeV, the electron flux has been varying (only) between about  $10^4$  and  $5 \cdot 10^5$  ( $\text{cm}^{-2} \text{s}^{-1} \text{sr}^{-1} \text{MeV}^{-1}$ ) with most frequent values around  $8 \cdot 10^4$  ( $\text{cm}^{-2} \text{s}^{-1} \text{sr}^{-1} \text{MeV}^{-1}$ ). Thereby, for that position and geomagnetic activity level, it can be concluded that the electron fluxes observed by EPT are reasonably compatible with AE8 Max predictions.

Fig. 17 shows the count rates in the electron physical channels (upper panel) and the corresponding unfolded differential spectra (lower panel), for 4 consecutive measurements at indicated times in a position bin located close to the slot region. In this case, the number of total counts/second is around 200 and the reconstruction of the incident spectra may show some non-natural fluctuations (see red histogram and the energy bin 0.6–0.7 MeV).

The situation only becomes critical when the total number of counts/second becomes close to 100 and when the PC4 or PC5 measures a count rate below 5 counts/second so that occasion-

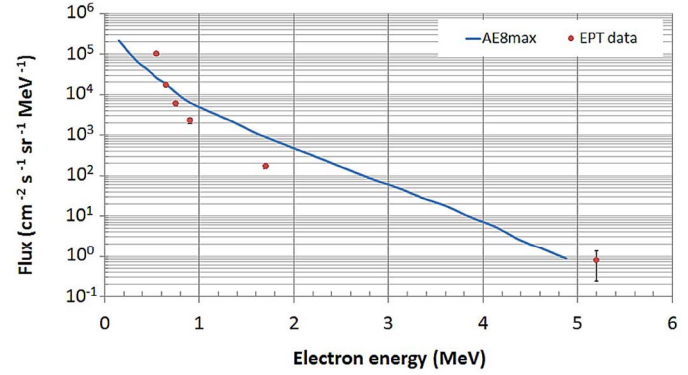


Fig. 16. Comparison between the differential flux as predicted by AE8MAX model and EPT results on 4th October 2013 (Geographic location: longitude =  $46.9^\circ$ , latitude =  $-55.8^\circ$ ; altitude = 831.2 km).

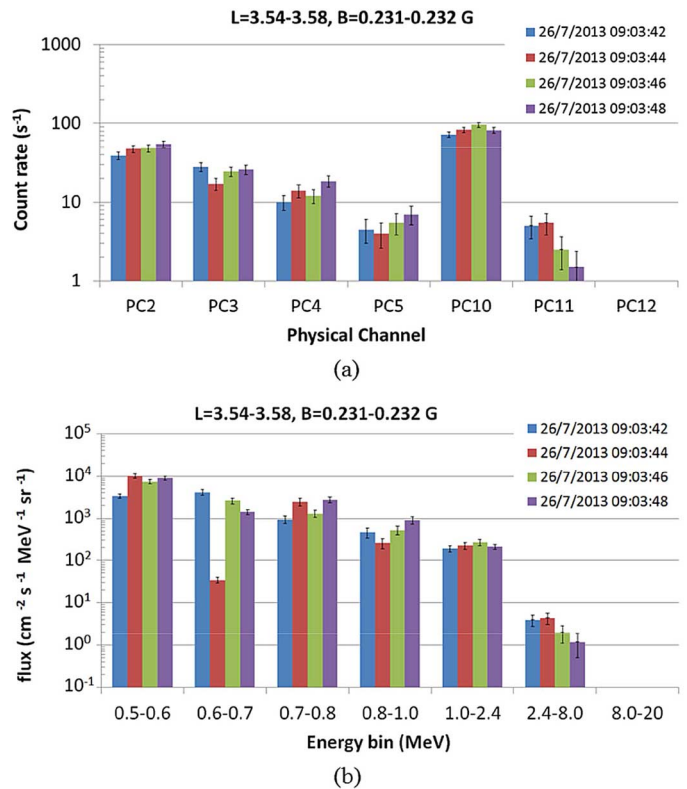


Fig. 17. (a) Physical channel spectra and (b) energy differential spectra (virtual channel spectra) as measured close to the slot region (Geographic location: latitude =  $-56.3^\circ \pm 0.2^\circ$ , longitude =  $12.3^\circ \pm 1^\circ$ ; altitude = 829.6 km).

ally these channels are not even filled at all due to statistical fluctuations. The reconstructed spectrum may then have an unphysical shape and in such cases only the average value over many passes in the area will be considered. Such situation is often observed at the edges of the outer radiation belt or the South Atlantic Anomaly (SAA).

While the strongly fluctuating spectra observed near the slot region have to be averaged before comparison with model predictions, they are quite suitable as single measurements for investigations of the physical processes involved in their dynamics and which affect their lifetimes.

Fig. 18 shows the time evolution of the differential flux for 0.5-0.6 MeV electrons, between 21 May and 23

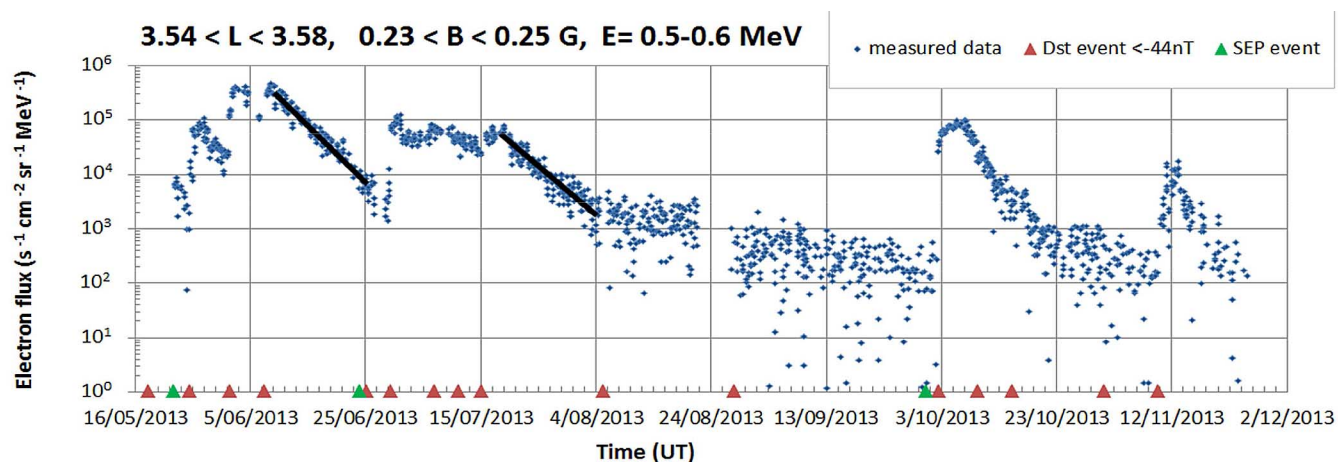


Fig. 18. Differential flux in the energy bin 0.5-0.6 MeV (blue dots) as a function of time for an indicated (L,B) bin. No averaging was done. The spread in data is mainly due to the spread of the counts in the unfolded spectra. The green triangles show the time of occurrence of a solar energetic particle event and the red triangles show the time of Dst minimum when a geomagnetic event occurred (only if Dst was below  $-44$  nT).

November 2013, for the indicated (L,B) range. The L, B coordinates were calculated with UNILIB v2.20 library (<http://trend.aeronomie.be/NEEDLE/unilib.html>). The field strength B is calculated using internal and external field models. The internal magnetic field component is calculated using the IGRF-2010 coefficients extrapolated to the date of measurement. To calculate the external field component the “Olsen-Pfitzer quiet” model was adopted. The McIlwain parameter L was determined using a magnetic dipole moment of  $M = 0.311653 \text{ GRe}^3$ .

It can be observed that after significant flux enhancement and the absence of strong geomagnetic activity during the following days, the flux decreases steadily following an exponential variation. Based on these flux data, electron lifetimes can be deduced as in [22] and compared to physical model predictions. Rough estimates based on both quiet periods in June and July give lifetimes of 4.5 days which is in agreement with  $T = 4.8 \pm 1.5$  days at  $L = 3.4 - 3.6$ ,  $B = 0.22 - 0.46 \text{ G}$  and  $E = 0.52 - 0.61 \text{ MeV}$  from reference [22].

A more detailed analysis of electron lifetimes at various positions is outside the scope of this paper. Lifetime calculation examples are provided herein to demonstrate that the quality of the EPT data, even in conditions of low count rates, makes these data suitable for detailed scientific investigations beyond the average radiation modeling purposes.

### B. Proton Spectra

Fig. 19 shows the measured counts in PCs and the unfolded differential spectra for 4 consecutive measurements inside a spatial bin located inside the SAA. The data were acquired with an EPT looking eastwards and an average boresight orientation of  $91^\circ$  with respect to the local magnetic field. The count rates in the original proton spectra rarely exceeds 400 counts/second as the proton flux is generally very low at that position of the proton radiation belt. Nevertheless, in the case of protons and He-ions, the spectra unfolding algorithm can cope with much lower statistics than in the case of electrons, due to the fact that the ion matrices are highly diagonal.

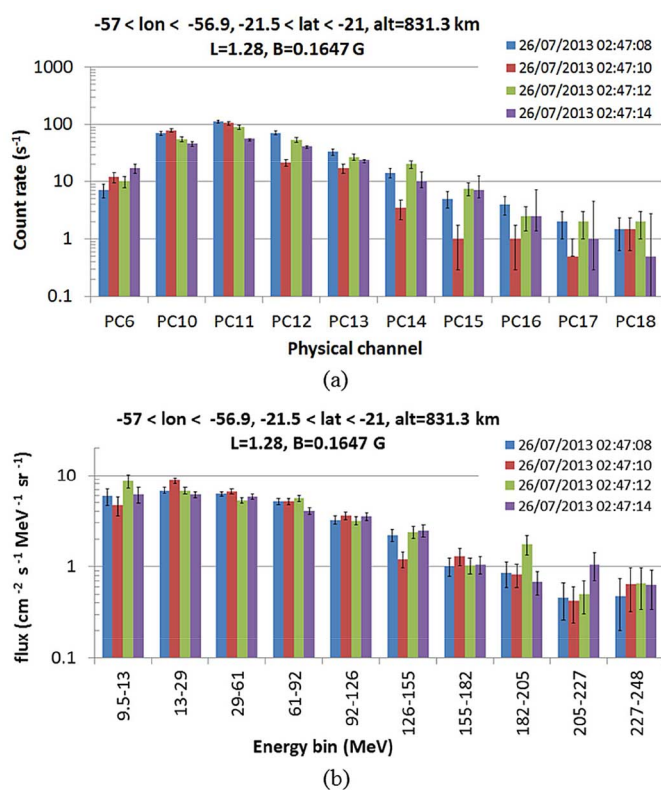


Fig. 19. (a) Counts in the EPT physical channels and corresponding (b) energy differential spectra as measured in the northern part of the SAA.

Proton fluxes in the SAA are known to be relatively stable and instantaneous measurements can be compared to model predictions, provided that uncertainties on single measurements are quoted. Fig. 20 shows a comparison between a measured spectrum with predictions from the AP8-MAX Unidirectional ( $PA = 90^\circ$ ) model accessed through SPENVIS. A rather good agreement is observed between measurements and AP8 model for  $\sim 100 \text{ MeV}$  protons. The agreement is less satisfactory in the 10–20 MeV energy range where the EPT single measurement is lower than AP8 predictions. The measured spectrum has

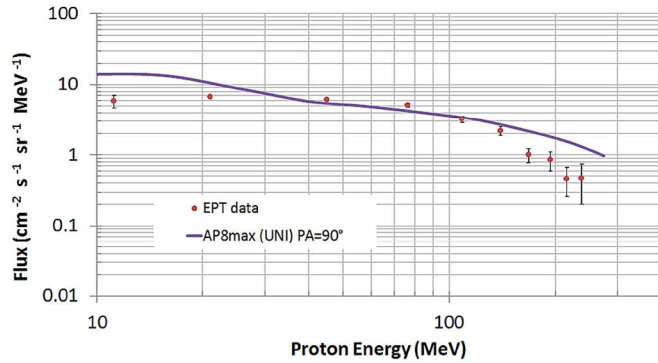


Fig. 20. Single proton spectrum measured by the EPT on 26 July 2013 with  $91^\circ$  average pitch angle, as compared to prediction of AP8-MAX Unidirectional for position: latitude =  $-21.5^\circ$ , longitude =  $-56.9^\circ$ , altitude = 831.3 km.

also a steeper slope for energies above 150 MeV. The statistical fluctuations are very high (see Fig. 19 upper panel) for these energies, but the quoted uncertainties on the EPT measurements lead to the conclusion that AP8 overestimates  $E > 150$  MeV protons at that position.

More details about comparisons of measured proton spectra with models and RPS/Van Allen Probes data can be found in [17]. Cross-validation of existing radiation models based on the EPT data and data from other science-class instruments is part of the data exploitation plan implemented at UCL/CSR in collaboration with partners worldwide.

Fig. 21 shows measured count rates and unfolded proton spectra acquired at high latitude (latitude =  $14^\circ \pm 3^\circ$ , longitude =  $72.15 \pm 0.15^\circ$ , altitude = 832.7 km), during a SEP event that started on 6th January 2014. Even though most of the detected protons have an energy  $E < 61$  MeV, the flux of low energy protons at high latitude was found to be an order of magnitude higher than that of protons stably trapped in the SAA. These protons are also found to be isotropically distributed i.e. no difference in intensity is observed for various instrument orientations. They are suitable for use in cross-calibrations of instruments that have different boresight directions as they fly within the above-indicated position.

### C. He-Ion Spectra

The EPT physical channels dedicated to He-ions do not usually record high statistics and the total number of counts in all the 11 considered He-ion physical channels is less than 10. Counts are only registered in the SAA, except during strong SEP events, when at high latitude, the number of counts may get as high as 10 in each of the two physical channels corresponding to the 38–116 MeV incident energy range. The long-term flux level maps are drawn by single measurement averaging over many passes across various position bins.

Fig. 22 shows a typical world map of the 615–720 MeV He-ion fluxes averaged over a bin of  $1^\circ$  latitude  $\times$   $1^\circ$  longitude for the time period 21 May–20 November 2013. It can be observed that in the SAA the highest averaged flux does not exceed  $10^{-2} \text{ cm}^{-2} \text{ s}^{-1} \text{ sr}^{-1} \text{ MeV}^{-1}$ , which corresponds to an average of about 0.4 count/second in the dedicated He-ion physical channel  $n^{\circ}7$ .

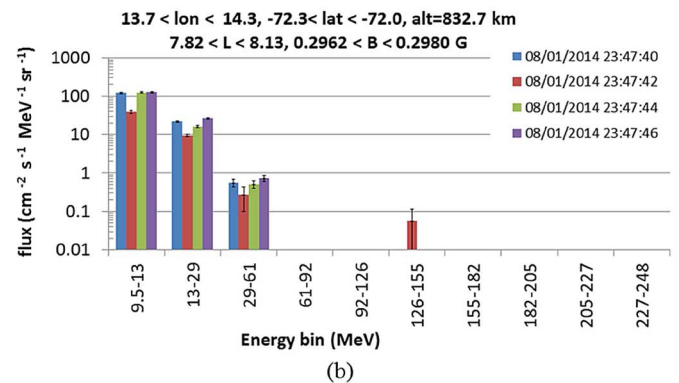
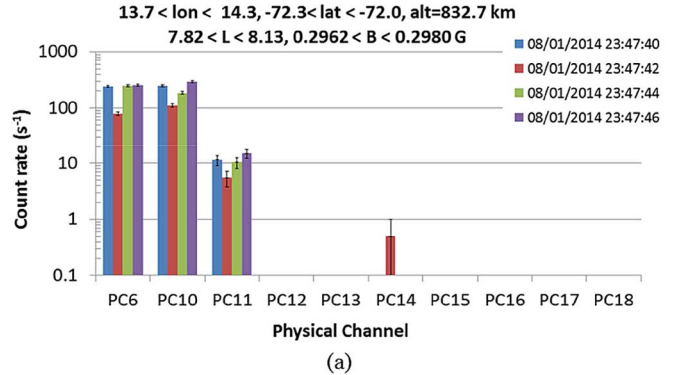


Fig. 21. (a) Physical channel spectra and (b) energy differential spectra (virtual channel spectra) as measured at high latitude during a SEP event.

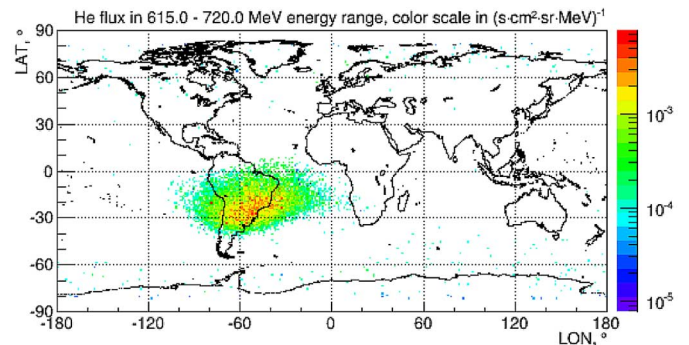


Fig. 22. World map (bin resolution  $1^\circ \times 1^\circ$ ) of average He-ion flux in the 615–720 MeV energy range measured by the EPT from 21 May 2013 to 20 November 2013.

## IV. THE EPT DATA ACCESS

The HTTP web page at the EPT Data Center [http://web.csr.ucl.ac.be/csr\\_web/probav/](http://web.csr.ucl.ac.be/csr_web/probav/) provides public access to a set of plots: particle spectra, geographical position, B-L parameters and instrument boresight orientation of measurements (FOV direction with respect to magnetic field giving the average particle pitch angle). It is dynamically updated and includes 6 tabs that can be selected. The names and the corresponding contents of each of these tabs are described hereafter:

- 1) “Home”: on the right side of the page an artistic view of PROBA-V satellite with EPT aperture window highlighted appears, and on the left side the following information are given: selected particle type, its energy, the current satellite position in geographical coordinate system and in B-L

coordinate system, for the given particle mean flux over all data measured at that position before, decay time of particle flux at current position (to be calculated), UTC time. Every 30 seconds this information is updated: the displayed particle and its energy are randomly selected, while the satellite position is updated according to the orbit predictions.

- 2) "Radiation Models": This page will contain steady state flux maps for electrons and protons, as well as lifetime maps (for details about these two products please refer to [23]). Comparisons to the existing radiation belt models AE-8, AP-8 and IRENE (INternational Radiation Environment Near Earth) will be presented as well. Right now all these links are not active yet, but work is in progress.
- 3) "Space Weather": This tab will be active by the end of the year 2014 upon completion of the space weather-related activities scheduled in the EPT data exploitation plan. It will provide access to time series of fluxes for selectable position, particle and energy; as well as to flux forecasting for the next few days, based on flux lifetime models.
- 4) "Event catalog": will contain information about special events that has occurred in the space radiation environment during EPT flight period.
- 5) "QL data" tab shows a set of Quick Look (QL) plots: electron, proton and alpha-particle fluxes, average pitch angle, geographical and B-L coordinates of measurements (the type of data to display can be selected in the "Select data to display:" menu). Only the ten latest measurement periods are selectable and this tab is updated automatically every time a new EPT data file is validated and processed at the EPT Data Center at UCL/CSR.
- 6) "Contacts" tab shows a list of contact persons who can provide further information on the EPT data.

There are 3 subsections at the bottom of each tab: "EPT news", "Proba-V news", "Data Access". "EPT news" updates periodically the link to one of the PDF documents containing latest information on EPT operations. "Proba-V news" points to the homepage of Proba-Vegetation instrument: <http://proba-v.vgt.vito.be>. "Data Access" is linked to the "QL data" tab that has been described above. Clicking on the EPT logo in the right top corner gives access to a web page that links to the EPT "instrument concept" article [9].

On request access can be given to numerical flux data set (L1 data) as well as to the full set of QL plots (time series plots of fluxes and other parameters including for example house-keeping data).

## V. CONCLUSION

Within this paper the characteristics and the functional performances of the PROBA-V EPT have been presented with as many details as may be required by the user of the EPT data. The provided information should allow the user to be aware not only of the unprecedented EPT capabilities to identify particle species, to cover wide energy ranges, to define accurate FOV, but also of the instrument limitations when count statistics become extremely low or when very high fluxes need slight corrections due to pulse pile-up.

In-flight particle discrimination capabilities make flux extractions so easy that the ready-to-use real-time flux data acquired

by the EPT can be exploited to forecast particle fluxes in space, making of the instrument an important tool for space-weather services.

The above-evoked cross-validation of the EPT data with radiation belt models and other science-class instruments like the ECT (Energetic particle, Composition and Thermal plasma) and RPS (Relativistic Proton Spectrometer) on board the Van Allen Probes will also be pursued in the context of the IRENE model collaboration as well as in other contexts aimed at improving space radiation models.

Combined with data from other instruments that are actually flying in space onboard various satellites, like the Van Allen Probes, Cluster, THEMIS, Giove-B, Proba-1, etc..., the EPT data are analyzed so as to contribute to further scientific understanding of the radiation dynamics processes in near-earth space.

## ACKNOWLEDGMENT

The entire manufacturer consortium thanks ESA for support of the development of the EPT and its accommodation on board PROBA-V. The EPT data exploitation team is also very grateful to the ESA/Redu MCC engineers and in particular to C. Bajot and E. Tilmans for the huge amount of work devoted to developing the required tools for flawless automated EPT operations. In addition, the authors are grateful to these latter team members as well as to D. Gerrits, K. Mellab, J. Naudet, and J. Van Hove for permitting early start of the commissioning phase and thus routine operation of the EPT as well as allowing off-pointing maneuvers. The CSR team also thanks P. Coquay, J. Nijskens, H. Verbeelen, and W. Verschueren at the Belgian Science Policy-Space Research and Applications (BELSPO) for support to the PRODEX project entitled "PROBA-V/EPT-Data Exploitation," ESA Contract C4000107617. It also thanks all the people who have participated to the construction of the EPT in an early stage of its development: C. Lippens, P. Leleux and many others that have brought temporary contribution to the project. The UCL/CSR team is also grateful to M. Kruglanski from BISA for providing the latest versions of IGRF in UNILIB. Special thanks to the PROBA-V/EPT team at B.USOC and QinetiQ Space for taking care of the data.

## REFERENCES

- [1] M. Walt, "Source and loss processes for radiation belt particles," in *Radiation Belts: Models and Standards*, J. F. Lemaire, D. Heynderickx, and D. N. Baker, Eds. Washington, DC: American Geophysical Union, 1996, pp. 1-13, Geophysical Monograph 97.
- [2] D. M. Fleetwood, P. S. Winokur, and P. E. Dodd, "An overview of radiation effects on electronics in the space telecommunications environment," *Microelectron. Reliab.*, vol. 40, no. 1, pp. 17-26, Jan. 2000.
- [3] S. Duzellier, "Radiation effects on electronic devices in space," *Aerosp. Sci. Technol.*, vol. 9, no. 1, pp. 93-99, Jan. 2005.
- [4] S. Gerardin, M. Bagatin, A. Paccagnella, G. Cellere, A. Visconti, and M. Bonanomi, "Impact of total dose on heavy-ion upsets in floating gate arrays," *Microelectron. Reliab.*, vol. 50, no. 9-11, pp. 1837-1841, Sep.-Nov. 2010.
- [5] E. Grossman and I. Gouzman, "Space environment effects on polymers in low earth orbit," *Nucl. Instrum. Methods Phys. Res. B*, vol. 208, pp. 48-57, Aug. 2003.
- [6] Y. Kimoto, N. Nemoto, H. Matsumoto, K. Ueno, T. Goka, and T. Omodaka, "Space radiation environment and its effects on satellites: Analysis of the first data from TEDA on board ADEOS-II," *IEEE Trans. Nucl. Sci.*, vol. 52, no. 5, pp. 1574-1578, Oct. 2005.

- [7] R. H. Maurer, M. E. Fraeman, M. N. Martin, and D. R. Roth, "Harsh environments: Space radiation environment, effects, and mitigation," *Johns Hopkins APL Tech. Dig.*, vol. 28, no. 1, pp. 17–29, 2008.
- [8] Y. Bentoutou and A. M. Si Mohammed, "A review of in-orbit observations of radiation-induced effects in commercial memories on-board alsat-1," *Int. J. Math. Comput. Phys. Quantum Eng.*, vol. 6, no. 6, pp. 13–15, 2012.
- [9] M. Cyamukungu and G. Grégoire, S. Fineschi and J. Fennelly, Eds., "The energetic particle telescope (EPT) concept and performances," in *Proc. SPIE 4 — Solar Physics and Space Weather Instrumentation*, Oct. 6, 2011, vol. 8148, ISBN: 9780819487582.
- [10] S. Agostinelli *et al.*, "GEANT4—A simulation toolkit," *Nucl. Instrum. Methods Phys. Res. A*, vol. 506, no. 3, pp. 250–303, Jul. 2003.
- [11] G. F. Knoll, "Radiation detection and measurement," in , 3rd ed. Hoboken, NJ, USA: Wiley, 2000, vol. 1, ISBN: 9780471073383.
- [12] M. Siegl, H. D. R. Evans, E. J. Daly, G. Santin, P. J. Nieminen, and P. Bühler, "Inner belt anisotropy investigations based on the standard radiation environment monitor (SREM)," *IEEE Trans. Nucl. Sci.*, vol. 57, no. 2, pp. 2017–2023, Apr. 2010.
- [13] M. Kruglanski and J. Lemaire, Trapped Proton Anisotropy at Low Altitudes, Tech. Note 6, TREND-3 Report, Apr. 1996.
- [14] H. M. Fischer, V. W. Auschrat, and G. Wibberenz, "Angular distribution and energy spectra of protons of energy  $5 \leq E \leq 50$  MeV at the lower edge of the radiation belt in equatorial latitudes," *J. Geophys. Res.*, vol. 82, no. 4, pp. 537–547, Feb. 1977.
- [15] J. Cabrera *et al.*, "Fluxes of energetic protons and electrons measured on board the oersted satellite," *Annales Geophysicae*, vol. 23, pp. 2975–2982, Nov. 2005.
- [16] J. D. Sullivan, "Geometrical factor and directional response of single and multi-element particle telescopes," *Nucl. Instrum. Methods*, vol. 95, no. 1, pp. 5–11, Aug. 1971.
- [17] S. Borisov *et al.*, "Angular distribution of protons measured by the energetic particle telescope on PROBA-V," *IEEE Trans. Nucl. Sci.*, to be published.
- [18] C. E. McIlwain, "Coordinates for mapping the distribution of magnetically trapped particles," *J. Geophys. Res.*, vol. 66, no. 11, pp. 3681–3691, Nov. 1961.
- [19] J. Cabrera and J. Lemaire, "Using invariant altitude ( $H_{inv}$ ) for mapping of the radiation belt fluxes in the low-altitude environment," *Space Weather*, vol. 5, no. S04007, Apr. 2007.
- [20] Belgian Institute for Space Aeronomy—Space Environment Information System (SPENVIS), ver. 4.6.7, Oct. 4, 2013 [Online]. Available: <https://www.spennis.oma.be/>
- [21] S. F. Fung, J. F. Lemaire, D. Heynderickx, and D. N. Baker, Eds., "Recent development in the NASA trapped radiation models," in *Radiation Belts: Models and Standards*. Washington, DC: American Geophysical Union, 1996, pp. 79–91, Geophysical Monograph 97.
- [22] S. Benck, L. Mazzino, M. Cyamukungu, J. Cabrera, and V. Pierrard, "Low altitude energetic electron lifetimes after enhanced magnetic activity as deduced from SAC-C and DEMETER data," *Annales Geophysicae*, vol. 28, pp. 848–859, Mar. 2010 [Online]. Available: <http://www.ann-geophys.net/28/849/2010/>
- [23] S. Benck, M. Cyamukungu, J. Cabrera, L. Mazzino, and V. Pierrard, "The transient observation-based particle (TOP) model and its potential application in radiation effects evaluation," *J. Space Weather Space Climate*, vol. 3, no. A03, pp. 1–10, 2013.